



Simultaneous X-Ray and Optical Polarization Observations of the Blazar Mrk 421

Athira M. Bharathan¹, C. S. Stalin², S. Sahayanathan^{3,4}, Kiran Wani^{5,6}, Amit Kumar Mandal⁷, Rwitika Chatterjee⁸, Santosh Joshi⁵, Jeewan C. Pandey⁵, Blesson Mathew¹, and Vivek K. Agrawal⁸

¹Department of Physics and Electronics, CHRIST (Deemed to be University), Bangalore, India; athira.bharathan@res.christuniversity.in, blesson.mathew@christuniversity.in

²Indian Institute of Astrophysics, Block II, Koramangala, Bangalore 560 034, India

³Astrophysical Sciences Division, Bhabha Atomic Research Centre, Mumbai-400085, India

⁴Homi Bhabha National Institute, Mumbai-400094, India

⁵Aryabhata Research Institute for Observational Sciences, Manora Peak, Nainital, India

⁶School of Physical Sciences, SRTM University, Nanded, 431 606, India

⁷Astronomy Program, Department of Physics and Astronomy, Seoul National University, Seoul 151-742, Republic of Korea

⁸Space Astronomy Group, ISITE Campus, U. R. Rao Satellite Centre, Bangalore 560 037, India

Received 2024 June 22; revised 2024 September 22; accepted 2024 September 24; published 2024 November 4

Abstract

We present near-simultaneous X-ray and optical polarization measurements in the high synchrotron peaked (HSP) blazar Mrk 421. The X-ray polarimetric observations were carried out using Imaging X-ray Polarimetry Explorer (IXPE) on 2023 December 6. During IXPE observations, we also carried out optical polarimetric observations using 104 cm Sampurnanand telescope at Nainital and multiband optical imaging observations using 2 m Himalayan Chandra Telescope at Hanle. From model-independent analysis of IXPE data, we detected X-ray polarization with degree of polarization (Π_X) of $8.5\% \pm 0.5\%$ and an electric vector position angle (Ψ_X) of $10^\circ.6 \pm 1^\circ.7$ in the 2–8 keV band. From optical polarimetry on 2023 December 6, in *B*, *V*, and *R* bands, we found values of $\Pi_B = 4.27\% \pm 0.32\%$, $\Pi_V = 3.57\% \pm 0.31\%$, and $\Pi_R = 3.13\% \pm 0.25\%$. The value of Π_B is greater than that observed at longer optical wavelengths, with the degree of polarization suggesting an energy-dependent trend, gradually decreasing from higher to lower energies. This is consistent with that seen in other HSP blazars and favors a stratified emission region encompassing a shock front. The emission happening in the vicinity of the shock front will be more polarized due to the ordered magnetic field resulting from shock compression. The X-ray emission, involving high-energy electrons, originates closer to the shock front than the optical emission. The difference in the spatial extension could plausibly account for the observed variation in polarization between X-ray and optical wavelengths. This hypothesis is further supported by the broadband spectral energy distribution modeling of the X-ray and optical data.

Unified Astronomy Thesaurus concepts: Active galactic nuclei (16); Blazars (164); BL Lacertae objects (158); X-ray sources (1822); Polarimetry (1278)

1. Introduction

Blazars are a unique category of active galactic nuclei (AGN) that are powered by accretion of matter onto supermassive black holes situated at the center of galaxies (D. Lynden-Bell 1969; N. I. Shakura & R. A. Sunyaev 1973; C. M. Urry & P. Padovani 1995). Their emission spans the accessible electromagnetic spectrum from low-energy radio to high-energy γ -rays (T. Hovatta & E. Lindfors 2019). The other observational properties of blazars include high bolometric luminosity, a two hump broadband spectral energy distribution (SED; G. Fossati et al. 1998), dominated by nonthermal emission, strong flux variability across the entire electromagnetic spectrum with timescale of variations ranging from minutes to hours (S. J. Wagner & A. Witzel 1995; M.-H. Ulrich et al. 1997), high degree of polarization in the radio and optical bands (J. R. P. Angel & H. S. Stockman 1980), optical polarization variability (I. Andruchow et al. 2005), and superluminal motion (C. M. Urry & P. Padovani 1995). These observational characteristics of blazars are likely due to their relativistic jets oriented close to the line of sight to the observer.

High synchrotron peaked (HSP) blazars, a subset of blazars, have the peak of their low-energy component occurring at frequencies greater than 10^{15} Hz in their broadband SED (A. A. Abdo et al. 2010). Blazars have been extensively studied using various diagnostics to understand the emission processes in them. Of these, multiwavelength linear polarization observations can serve as an efficient tool to constrain blazar emission. Such an investigation can provide the needed constraints on the particle acceleration processes in blazar jets. Polarization observations have historically been accessible at radio, infrared, and optical wavelengths; new developments in the X-ray range have enabled the detection of X-ray polarization with the launch of the Imaging X-ray Polarimetry Explorer (IXPE; M. C. Weisskopf et al. 2022) satellite, which began its scientific operations in 2022 January.

The BL Lac object Mkn 421 is one of the closest ($z = 0.031$) and broadly examined blazars with a nonthermal spectrum spanning from radio to very high-energy gamma-rays (V. A. Acciari et al. 2009). Given its status as the brightest HSP blazar at X-ray energies, Mrk 421 presents an ideal target for polarization measurements using IXPE (L. Di Gesu et al. 2023). Hence, this source has been observed by IXPE multiple times (L. Di Gesu et al. 2022, 2023; D. E. Kim et al. 2024). Such X-ray observations can be used to probe the region of the jet where the flow is accelerated and collimated. This paper

reports the results of simultaneous X-ray and optical polarization observations of Mrk 421 on 2023 December 6. This paper is structured as follows. Section 2 covers the observations and data reduction. The analysis and results are presented in Section 3, followed by the discussion in Section 4. The final section (Section 5) provides a summary.

2. Observations and Data Reduction

2.1. X-Ray Polarization

The blazar Mrk 421 has been observed multiple times using IXPE since 2022 May (L. Di Gesu et al. 2022, 2023; S. Ehlert 2023; D. E. Kim et al. 2024). This study focuses on a recent observation conducted on 2023 December 6 (OBSID: 02008199), with IXPE, for a net exposure time of 70,751 s. Cleaned and calibrated level 2 data were used in our scientific analysis. Using IXPEOBSSIM software version 30.0.0 (L. Baldini et al. 2022), we performed the analysis using publicly available data. We utilized the CMAP method in the xpbins task to generate a counts map in sky coordinates. For source extraction, we utilized a circular region with a radius of 60'' across all three Detector Units (DUs). For background extraction in each DU, we employed a source-free annular region with an inner radius of 100'' and an outer radius of 300''. Subsequently, the xpselect task was utilized to create filtered source and background regions for polarimetric analysis.

2.2. Optical Polarization

Optical polarimetric observations were carried out with the ARIES Imaging Polarimeter (AIMPOL) mounted on the 104 cm Sampurnanand Telescope, Nainital. AIMPOL is a dual-channel polarimeter forming an extraordinary and ordinary image of a single object on the CCD (B. S. Rautela et al. 2004; J. C. Pandey et al. 2023). Four different half-wave plate (HWP) rotation (i.e 0°, 22.5°, 45° and 67.5°) measurements are required in AIMPOL. Stokes parameters for each rotation angle were calculated as follows:

$$R(\alpha) = \frac{\left(\frac{I_e(\alpha)}{I_o(\alpha)} - 1 \right)}{\left(\frac{I_e(\alpha)}{I_o(\alpha)} + 1 \right)} \quad (1)$$

where $I_e(\alpha)$ and $I_o(\alpha)$ are the intensities of the extraordinary and ordinary images, respectively, of the source at four different HWP rotation angles (α). Since the response of the CCD is not the same for extraordinary and ordinary images of the object, the flux ratio $\frac{I_e(\alpha)}{I_o(\alpha)}$ was multiplied by a factor F and it is expressed as (A. N. Ramaprakash et al. 1998):

$$F = \left[\frac{I_o(0^\circ) \times I_o(22.5^\circ) \times I_o(45^\circ) \times I_o(67.5^\circ)}{I_e(0^\circ) \times I_e(22.5^\circ) \times I_e(45^\circ) \times I_e(67.5^\circ)} \right]^{1/4}. \quad (2)$$

Normalized four Stokes parameters corresponding to each HWP rotation angle (i.e., $R(0^\circ) \sim q$, $R(22.5^\circ) \sim u$, $R(45^\circ) \sim q_1$, and $R(67.5^\circ) \sim u_1$) were used to calculate the degree of polarization P and the polarization position angle θ . P was calculated from an average of $p_1 = \sqrt{q^2 + u^2}$ and $p_2 = \sqrt{q_1^2 + u_1^2}$, similarly θ was calculated from an average of $\theta_1 = 0.5 \times \tan^{-1}\left(\frac{u}{q}\right)$ & $\theta_2 = 0.5 \times \tan^{-1}\left(\frac{u_1}{q_1}\right)$. Aperture photometry using the *astropy* package-*photutils* was used to obtain

Table 1
The Log of Optical Polarization Observations

Date	Number of Observations		
	<i>B</i>	<i>V</i>	<i>R</i>
02/12/2023	0	0	3
05/12/2023	3	3	3
06/12/2023	3	3	6
07/12/2023	3	3	42
02/01/2024	3	3	3
03/01/2024	3	3	3

Note. Given are the dates of observations and the number of images acquired in *B*, *V* and *R* filters.

the flux values of the extraordinary and ordinary images of the source. We observed unpolarized and polarized standard stars during each observation night and used them, respectively, to correct instrumental polarization and in zero-point calibration of the position angle (PA). HD19820 and HD245310 were observed as standard polarized stars, while G191B2B and HD14069 were observed as standard unpolarized stars (G. D. Schmidt et al. 1992). We observed the source on six epochs between 2023 December 2 and 2024 January 3, the details of which are given in Table 1.

2.3. Optical Imaging

Optical imaging observations were carried out in u' , g' , r' , and i' filters on 2023 December 5, using the 2 m Himalayan Chandra Telescope. The observed optical data were reduced using the Image Reduction and Analysis Facility (IRAF; D. Tody 1993, 1986), following standard procedures, including bias subtraction, dark subtraction, flat-fielding, and cosmic ray removal. Following reduction, objects within the observed image frames were identified utilizing the *daofind* task within IRAF. Subsequently, photometry was conducted on these detected objects using the *phot* task in IRAF. From the detected objects, several comparison stars from the same field of view (FoV) were selected to perform differential photometry to bring the instrumental magnitude obtained for Mrk 421 to the standard system. For this aperture, photometry was performed with an aperture size three times the seeing size, typically ranging from 4''4 to 6''2 in u' , g' , r' , and i' filters. Notably, the aperture size chosen for photometry of Mrk 421 excludes the nearby galaxy (LEDA 33453). For differential photometry the apparent magnitudes of the comparison stars were taken from the SDSS DR18 sky survey⁹ in the respective filters.

2.4. Swift-XRT

To generate the X-ray spectral data points needed to construct the SED, we used observations from the X-Ray Telescope (XRT; D. N. Burrows et al. 2005) onboard the Neil Gehrels Swift Observatory.¹⁰ These observations were conducted simultaneously with IXPE on 2023 December 6 (OBSID: 00097201001). We processed the XRT data using the *xrtpipeline*¹¹ task available in the HEASOFT software package.¹² The data was extracted in the 0.5–10 keV energy

⁹ <https://skyserver.sdss.org/dr18/VisualTools/explore/summary>

¹⁰ <https://heasarc.gsfc.nasa.gov/cgi-bin/W3Browse/swift.pl>

¹¹ <https://www.swift.ac.uk/analysis/xrt/xrtpipeline.php>

¹² <https://heasarc.gsfc.nasa.gov/docs/software/heasoft/>

Table 2

Results of the X-Ray polarization observations on 2023 December 6 (OBSID = 02008199)

	2–3 (keV)	3–5 (keV)	5–8 (keV)	2–8 (keV)
Π_X (%)	7.6 ± 0.6	10.1 ± 0.7	8.2 ± 1.9	8.5 ± 0.5
Ψ_X (deg)	12.3 ± 2.4	10.4 ± 2.0	24.5 ± 6.9	10.6 ± 1.7
MDP (%)	1.95	2.11	5.94	1.52

Note. Here, MDP is the minimum detectable polarization.

range. For the source extraction, we defined an annular region with inner and outer radii of $60''$ and $80''$, respectively. For background extraction, we selected a circular region of radius $70''$ away from the source. The ancillary response file (ARF) was generated using the *xrtrmkarf* task. We then used the *grppha* tool to group the spectra, ensuring that each energy bin contained at least 20 counts. For spectral fitting, we applied an absorbed power-law model. The Galactic hydrogen column density (N_H) was fixed at $1.34 \times 10^{20} \text{ cm}^{-2}$ (HI4PI Collaboration et al. 2016).

3. Analysis and Results

3.1. X-Ray Polarization

We analyzed the polarimetric signal from Mrk 421 using PCUBE algorithm in the *xpbin* task. We generated three polarization cubes for the three DUs to extract information, including the polarization degree (Π_X) and the polarization angle (Ψ_X). The combined polarization parameters from the three DUs in the 2–3 keV, 3–5 keV, 5–8 keV, and the total 2–8 keV bands are given in Table 2. The polarization degree Π_X is found to be $8.5\% \pm 0.5\%$ in the 2–8 keV band with $\Psi_X = 10.6 \pm 1.7$ deg. In addition, there is an increase in the Π_X from 2–3 keV to 3–5 keV. The normalized U/I and Q/I Stokes parameters obtained from the combined cube in different energy bands are shown in Figure 1. We also carried out spectropolarimetric (model-dependent polarization) analysis. We considered Galactic absorption along the line of sight to Mrk 421 by using the *TBabs* model with a weighted average column density (N_H) from HI4PI Collaboration et al. (2016). The N_H value was fixed at $1.34 \times 10^{20} \text{ cm}^{-2}$ during the fit. For spectral modeling, we employed a simple power-law model (*pow*), and for modeling X-ray polarization, we used the *polconst* model based on Stokes parameters. In XPSEC, the model is expressed as:

$$\text{constant} \times \text{TBabs} \times (\text{polconst} \times \text{pow}). \quad (3)$$

Here, constant represents the intercalibration constant for each detector. We achieved statistically acceptable fits with a χ^2/dof value of 1.3.

The polarization degree Π_X is found to be $9.5\% \pm 1.2\%$ in the 2–8 keV band with Ψ_X of 11.1 ± 3.8 deg. Both methods thus gave consistent results within errors. For the comparison, the derived model-independent and dependent values are given in Table 3. The position of the measured polarization values in the Π_X and Ψ_X plane in the 2–8 keV band for PCUBE and XSPEC analysis are given in Figure 1. In addition, the PD change in different energy bands for IXPE analysis is given in Figure 1.

3.2. Optical Polarization

Using AIMPOL, we found optical polarization in the *B*, *V*, and *R* bands. On 2023 December 6, optical polarization degree (Π_O) was found to be $4.27\% \pm 0.32\%$, $3.57\% \pm 0.31\%$, and $3.13\% \pm 0.25\%$ in *B*, *V*, and *R* filters, respectively. In the optical band, we also found an increase in the polarization degree with energy. The results on all optical observations are given in Table 4. The optical polarization degree and polarization angle for each filter are given in the bottom right panel of Figure 1 while the results on all the optical band polarization are given in Figure 2.

4. Discussion

Simultaneous optical and X-ray polarization measurements are pivotal in unveiling the underlying emission mechanisms and particle acceleration processes in high-energy sources such as blazars. For Mrk 421, a source with multiple X-ray polarization measurements, we conducted a comparison with the values obtained on 2023 December 6 against previous observations (L. Di Gesu et al. 2022, 2023; S. Ehlert 2023; D. E. Kim et al. 2024). All the available X-ray polarization values of Mrk 421 are given in Table 5. Earlier observations indicate that the degree of X-ray polarization for Mrk 421 ranges from 10% to 15%. However, on 2023 December 6, the degree of polarization was found to be 8.5%, the lowest among all the observations. Interestingly, the analysis conducted on 2022 December 6 (ID: 02004401) by D. E. Kim et al. (2024) revealed a Π_X of $14\% \pm 1\%$ and a ψ_X of $107^\circ \pm 3^\circ$, with a net exposure time of 74 ks. During this period, the source was in a typical X-ray activity state, exhibiting an X-ray flux of $2.8 \times 10^{-10} \text{ erg cm}^{-2} \text{ s}^{-1}$ in the 2–8 keV band. In contrast, our analysis of Mrk 421 on 2023 December 6 (ID: 02008199) with a net exposure time of 70 ks showed a lower Π_X of $8.5\% \pm 0.5\%$ and a significantly different ψ_X of 10.6 ± 1.7 degrees. During this observation, the source exhibited a higher X-ray flux of $3 \times 10^{-10} \text{ erg cm}^{-2} \text{ s}^{-1}$ in the 2–8 keV band, indicating a state of elevated X-ray activity. This difference in polarization characteristics and X-ray flux suggests a possible change in the magnetic field structure or emission region within the blazar, reflecting the dynamic nature of high-energy processes in Mrk 421. To obtain further insights into the emission processes, we carried out the broadband modeling of its SED using synchrotron and inverse Compton mechanisms.

Our model assumes the emission region to be located around a shock front. The electrons are accelerated in the vicinity of the shock front and advected into the jet medium while losing their energy through radiative processes. Due to shock compression, the magnetic field lines close to the shock front will be more ordered and transverse to the flow direction, whereas they may be tangled at regions farther away. Hence, the synchrotron emission happening in the vicinity of the shock front will be more polarized than the farther regions. Since the X-ray emission involves high-energy electrons, the emission will be confined within the vicinity of the shock and will be more polarized. On the other hand, optical/UV emitting electrons demand less energy and can advect to farther regions resulting in less polarized emission. This scenario accounts for the difference in polarization measurements observed in optical and X-ray energies. A schematic of the model considered here is shown in the left-hand panel of Figure 3.

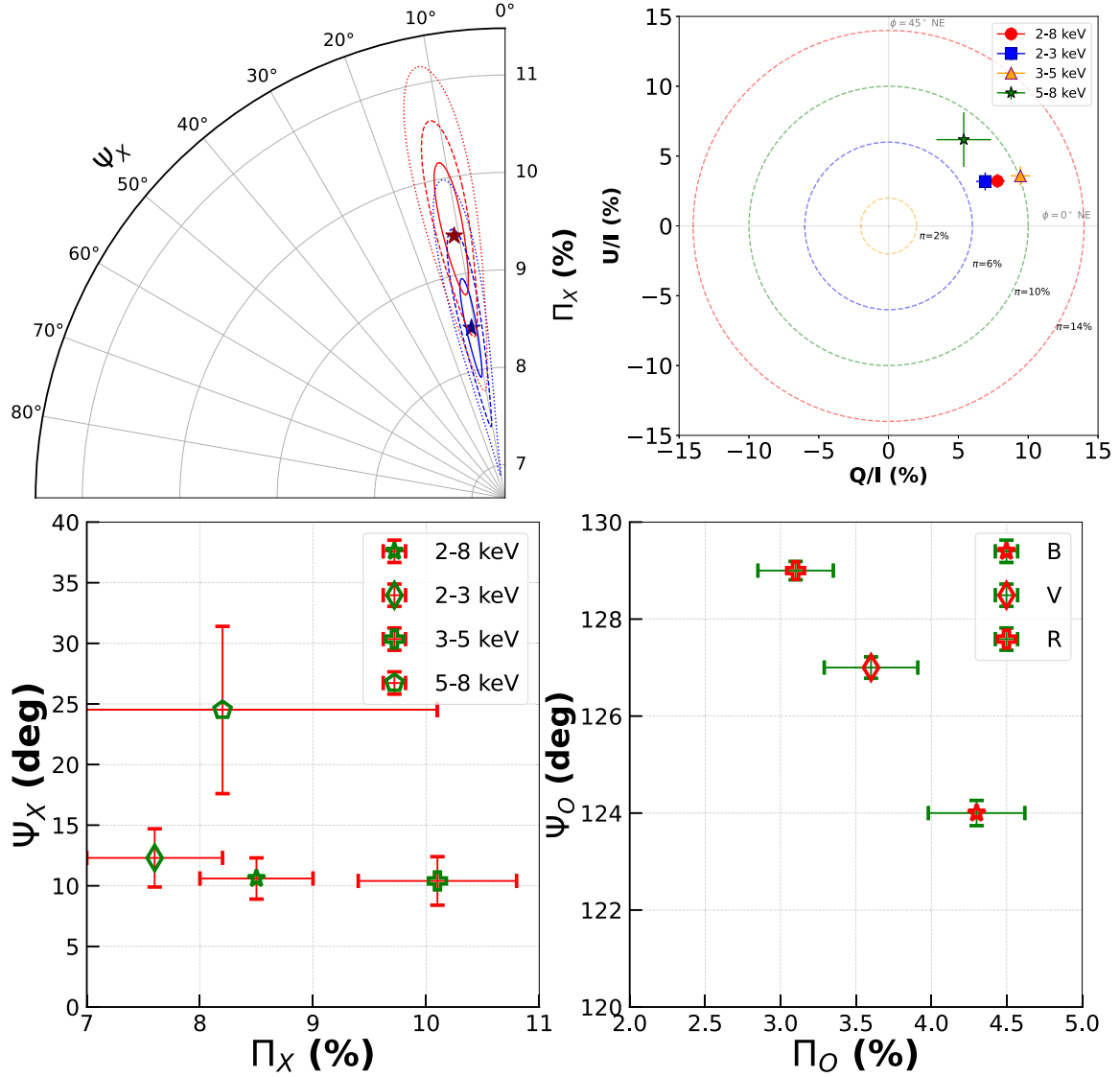


Figure 1. Results of the optical and X-ray polarization measurements on 2023 December 6. Top left-hand panel: Position of the 2–8 keV X-ray polarization in the Π_X - Ψ_X plane obtained using PCUBE (blue star) and XSPEC analysis (red star). Top right-hand panel: The normalized U/I and Q/I Stokes parameter in the total 2–8 keV (red circle), 2–3 keV (blue square), 3–5 keV (orange triangle), and 5–8 keV (green star). Bottom left-hand panel: The measured X-ray polarization in Π_X - Ψ_X plane. Here, the star represents 2–8 keV, the diamond represents 2–3 keV, a plus represents 3–5 keV, and the pentagon represents 5–8 keV. Bottom right-hand panel: The measured optical polarization (Π_O) in B band (star), V band (diamond) and R band (plus).

To model the total synchrotron emission arising from this region, we denote the location of the shock front as z_0 and the accelerated electron distribution as

$$n(\gamma, z_0) = k\gamma^{-p} \quad \text{for } \gamma < \gamma_{\max} \quad (4)$$

where p is the particle index. Due to synchrotron loss, the distribution at a distance z from z_0 will be

$$n(\gamma, z) = \frac{\bar{P}(\Gamma_z)}{\bar{P}(\gamma)} n(\Gamma_z, z_0) \quad (5)$$

where Γ_z is the Lorentz factor of the electron at z_0 which reduces to γ at z and \bar{P} is the spatial energy loss. For a constant advection, we can express

$$\begin{aligned} \bar{P}(\gamma) &= \frac{d\gamma}{dz} = \left(\frac{d\gamma}{dt} \right) / \left(\frac{dz}{dt} \right) \\ &= -\xi\gamma^2 \end{aligned} \quad (6)$$

Table 3
The Measured Polarization Parameters from Model-independent and Spectropolarimetry Analysis in the 2–8 KeV Band

OBSID	Model Independent		Spectropolarimetry	
	Π_X (%)	Ψ_X (deg)	Π_X (%)	Ψ_X (deg)
02008199	8.5 ± 0.5	10.6 ± 1.7	9.5 ± 1.2	11.1 ± 3.8

and hence,

$$n(\gamma, z) = \frac{\Gamma_z^2}{r^2} n(\Gamma_z, z_0). \quad (7)$$

Using Equation (6), Γ_z can be expressed as

$$\int_{z_0}^z dz = - \int_{\Gamma_z}^{\gamma} \frac{dx}{\xi x^2} \quad (8)$$

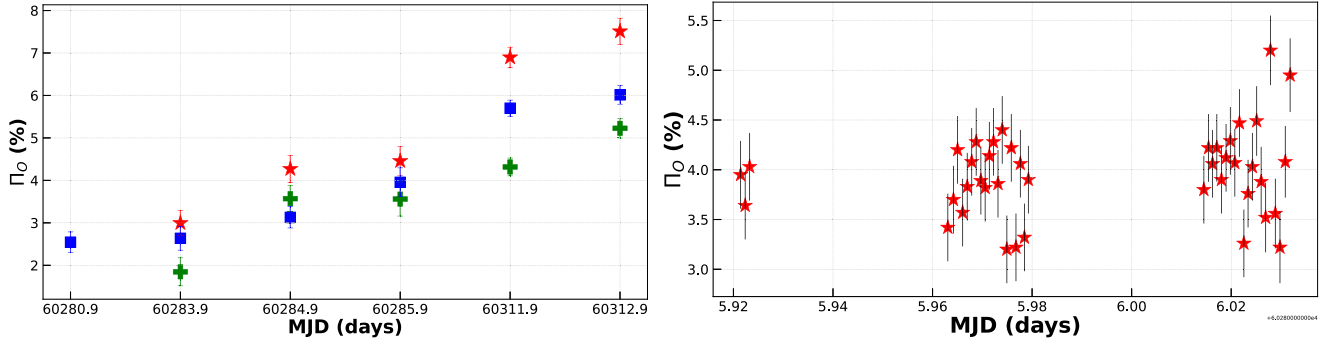


Figure 2. Left-hand panel: The measured mean optical polarization degree in B (star), V (plus), and R (square) filters, for all the epochs of observations (see Table 5). Right-hand panel: R -band measurements ($n = 42$) from 2023 December 7, demonstrating significant variability in the degree of polarization over the course of a single night.

Table 4
The Results of Optical Polarization Observations

Date	B			V			R		
	N	PD	PA	N	PD	PA	N	PD	PA
02/12/2023	3	2.55 ± 0.24	82.9 ± 0.19
05/12/2023	3	2.99 ± 0.29	124.0 ± 0.27	3	1.85 ± 0.33	91.2 ± 0.23	3	2.64 ± 0.28	82.7 ± 0.21
06/12/2023	3	4.27 ± 0.32	124.0 ± 0.26	3	3.57 ± 0.31	127.7 ± 0.22	6	3.13 ± 0.25	129.1 ± 0.19
07/12/2023	3	4.46 ± 0.34	120.5 ± 0.28	3	3.56 ± 0.40	80.9 ± 0.25	42	3.96 ± 0.34	124.8 ± 0.23
02/01/2024	3	6.89 ± 0.24	132.2 ± 0.42	3	4.32 ± 0.21	140.4 ± 0.41	3	5.70 ± 0.19	125.7 ± 0.41
03/01/2024	3	7.51 ± 0.31	142.8 ± 0.43	3	5.23 ± 0.23	138.1 ± 0.42	3	6.01 ± 0.22	128.4 ± 0.41

Note. Here, N is the number of observations, PD is the polarization degree in percentage, and PA is the position angle in degrees. The quoted polarization PD and PA are the average of the N measurements.

Table 5

Summary of X-Ray Polarization Observations Available for Mrk 421 Until 2023 December

Obs. Date	Π_x (%)	References
2022-05-04	15 ± 2	L. Di Gesu et al. (2022)
2022-06-04	10 ± 1	L. Di Gesu et al. (2023)
2022-06-07	10 ± 1	L. Di Gesu et al. (2023)
2022-12-06	14 ± 1	D. E. Kim et al. (2024)
2023-12-06	8.5 ± 0.5	This work

Note. The date of observation and the measured degree of polarization is given.

and we get

$$\Gamma_x = \left[\frac{1}{\gamma} - \xi(z - z_0) \right]^{-1}. \quad (9)$$

Similarly, the extension of the region encompassing the electrons of Lorentz factor γ can be found as

$$z_{\max}(\gamma) = z_0 + \frac{1}{\xi} \left[\frac{1}{\gamma} - \frac{1}{\gamma_{\max}} \right]. \quad (10)$$

The total number of electrons with Lorentz factor γ will then be

$$N_{\text{tot}}(\gamma) = \pi R^2 \int_{z_0}^{z_{\max}(\gamma)} n(\Gamma_x, z_0) dx \quad (11)$$

where the jet is assumed to be cylindrical with radius R . The synchrotron flux received on earth is then obtained by convolving Equation (11) with the single particle emissivity

(G. B. Rybicki & A. P. Lightman 1986). Due to the relativistic motion of the jet, the observer will see an enhanced emission modulated by the Doppler factor (δ) and the observed flux after accounting for the cosmological effects will be (C. D. Dermer 1995),

$$F_{\text{obs}}(\nu_{\text{obs}}) = \frac{\delta_D^3 (1+z)}{d_L^2} V j_{\text{syn}} \left(\frac{1+z}{\delta_D} \nu_{\text{obs}} \right) \times \text{erg cm}^{-2} \text{s}^{-1} \text{Hz}^{-1} \quad (12)$$

where z is the redshift of the source, d_L is the luminosity distance, V is the volume of the emission region, and j_{syn} is the emissivity due to the synchrotron process.

The model is applied on the simultaneous SED obtained on 2023 December 6. The X-ray data was reduced from the Swift-XRT observation and the optical data was obtained from the observation using HCT. The fluxes in u' , g' , r' , and i' were used to construct the SED. The observed optical–X-ray flux points are shown in Figure 3 (right-hand panel) along with the model curve. The model can reproduce the observed SED well and the main parameters are given in Table 6. To obtain insight into the observed difference in the optical and X-ray polarization measurements, we study the extension of the regions using the model parameters. The Lorentz factor of the electrons responsible of the observed emission at ν_{obs} will be (G. B. Rybicki & A. P. Lightman 1986),

$$\nu_{\text{obs}} = \frac{\delta}{1+z} \gamma^2 \frac{eB}{2\pi mc} \quad (13)$$

where B is the magnetic field. Using the parameters provided in Table 6, we find the electron Lorentz factors responsible

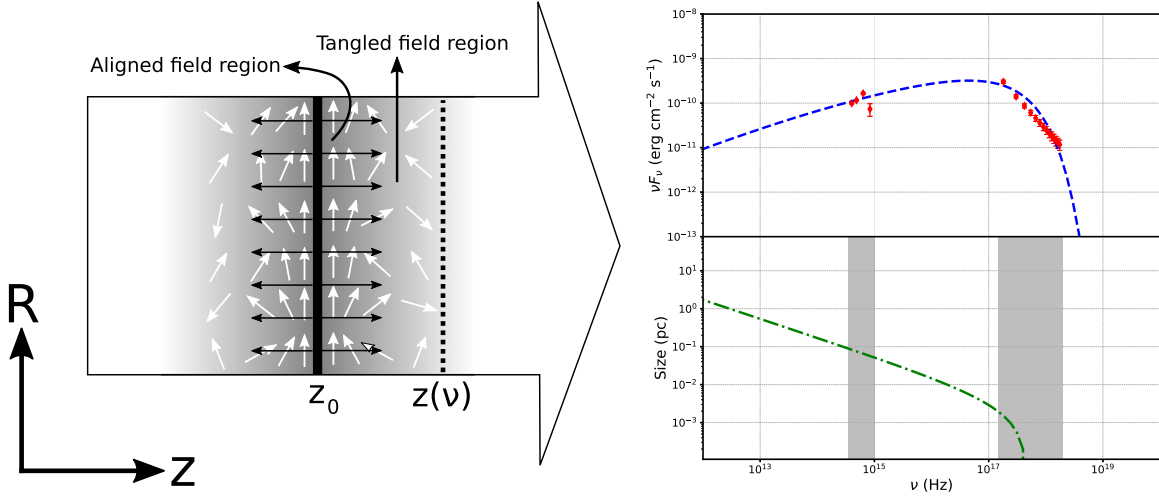


Figure 3. The left-hand panel illustrates the emission regions characterized by different magnetic field configurations: an aligned magnetic field at position z_0 , where X-ray emission originates, and a tangled magnetic field at position $z(v)$, which is the source of optical emission. The right-hand panel consists of two subplots: the top subplot shows the model fit (blue dotted line) to the observed optical and X-ray emissions, while the bottom subplot indicates the spatial extension of their respective emission regions (green dotted line).

Table 6

The Model Parameters for the SED Shown in Figure 3 for the Epoch of 2023 December 6

Parameter	Values
R (cm)	1.2×10^{15}
B (G)	0.1
δ	19
p	1
k ($\# \text{ cm}^{-3}$)	1

Note. The advection velocity is assumed to be c .

for optical and X-ray emission are $\gamma_o = 8801.39$ and $\gamma_X = 582156.99$. The extension of the emission region can then be estimated using Equation (10) as $z_o = 8.56 \times 10^{-2}$ pc and $z_X = 1.29 \times 10^{-3}$ pc. We find the optical and X-ray emitting regions differ by ~ 0.1 pc. If we attribute the decrease in optical polarization as a result of tangling of the field lines at regions farther from the shock front, then the disordering of the field lines happens typically at a length scale of ~ 0.1 pc.

5. Summary

Mrk 421 is one of the sources observed multiple times by IXPE. The new X-ray polarization observation of this source along with simultaneous optical polarization were studied in this work. From our analysis, we arrived at the following conclusions.

1. We found significant X-ray polarization value of $\Pi_X = 8.5\% \pm 0.05\%$ and $\psi_X = 10^{\circ}6 \pm 1^{\circ}7$ in the 2–8 keV band from model-independent analysis. This is lower than that observed from the source at earlier epochs of observations.
2. From model-dependent analysis we found $\Pi_X = 9.5\% \pm 1.2\%$ and $\psi_X = 11^{\circ}1 \pm 3^{\circ}8$. This is in agreement with the values obtained from model-independent analysis.
3. In the optical band we found the polarization degree to range from 3.13% to 4.27% for different filters and this

value is found to increase with energies. In addition, Π_X is found to be larger compared to optical wavelengths. Among X-rays too, we found Π_X to increase with energy between 2–3 keV and 3–5 keV, but drops again in the 5–8 keV with a large error that makes the value in the 5–8 keV band consistent with the values both at the 2–3 keV and 3–5 keV bands. Not considering the polarization degree in the 5–8 keV band due to the large error in the measurement, we found an energy dependent polarization from simultaneous observations in optical and X-ray energies. This is similar to that seen in other blazars, such as Mrk 501 (X.-K. Hu et al. 2024) and 1ES 0229+200 (S. R. Ehlert et al. 2023).








4. Our observations suggest a spatial gradient in the maximum available particle energy within the emission region. This variation in particle energy could potentially explain the observed temporal changes in polarization. This finding aligns with observations of HSP blazars, where studies have shown higher-energy emission exhibiting larger-amplitude polarization variations compared to lower-energy bands.
5. The lower optical polarization compared to X-ray shows that electrons are accelerated in the shock front, the high-energy X-rays originate close to the shock front with the optical originating at much larger distances down the jet. SED modeling assuming such a scenario suggests the disordering of the magnetic field lines happens typically on a length scale of ~ 0.1 pc from the shock (main acceleration zone).

Acknowledgments

We thank the anonymous referee for their valuable feedback, which has significantly enhanced the quality of this manuscript. The Imaging X-ray Polarimetry Explorer (IXPE) is a joint US and Italian mission. The US contribution is supported by the National Aeronautics and Space Administration (NASA) and is led and managed by its Marshall Space Flight Center (MSFC), with industry partner Ball Aerospace (contract NNM15AA18C). The Italian contribution is supported by the Italian Space Agency (Agenzia Spaziale Italiana, ASI) through contract ASI-OHBI-

2017-12-I.0, agreements ASI-INAF-2017-12-H0 and ASI-INFN-2017.13-H0, and its Space Science Data Center (SSDC) with agreements ASI-INAF-2022-14-HH.0 and ASI-INFN 2021-43-HH.0, and by the Istituto Nazionale di Astrofisica (INAF) and the Istituto Nazionale di Fisica Nucleare (INFN) in Italy. This research used data products provided by the IXPE Team (MSFC, SSDC, INAF, and INFN) and distributed with additional software tools by the High-Energy Astrophysics Science Archive Research Center (HEASARC), at NASA Goddard Space Flight Center (GSFC). We acknowledge the use of the Himalayan Chandra Telescope (HCT) at the Indian Astronomical Observatory, Hanle, and the ARIES Imaging Polarimeter (AIMPOL) at the Aryabhata Research Institute of Observational Sciences (ARIES), Nainital, India, to obtain the data presented in this work. We extend our gratitude to the staff and researchers at the Indian Institute of Astrophysics (IIA) and ARIES for their support and maintenance of these facilities. A.M.B expresses gratitude to the Department of Science and Technology (DST) for the INSPIRE Fellowship (IF200255).

ORCID iDs

Athira M. Bharathan  <https://orcid.org/0009-0009-0416-6829>
 C. S. Stalin  <https://orcid.org/0000-0002-4998-1861>
 Kiran Wani  <https://orcid.org/0000-0003-0841-7823>
 Amit Kumar Mandal  <https://orcid.org/0000-0001-9957-6349>
 Santosh Joshi  <https://orcid.org/0009-0007-1545-854X>
 Jeewan C. Pandey  <https://orcid.org/0000-0002-4331-1867>
 Blesson Mathew  <https://orcid.org/0000-0002-7254-191X>

References

- Abdo, A. A., Ackermann, M., Agudo, I., et al. 2010, *ApJ*, 716, 30
 Acciari, V. A., Aliu, E., Aune, T., et al. 2009, *ApJ*, 703, 169
 Andruchow, I., Romero, G. E., & Cellone, S. A. 2005, *A&A*, 442, 97
 Angel, J. R. P., & Stockman, H. S. 1980, *ARA&A*, 18, 321
 Baldini, L., Bucciantini, N., Lalla, N. D., et al. 2022, *SoftX*, 19, 101194
 Burrows, D. N., Hill, J. E., Nousek, J. A., et al. 2005, *SSRv*, 120, 165
 Dermer, C. D. 1995, *ApJL*, 446, L63
 Di Gesu, L., Donnarumma, I., Tavecchio, F., et al. 2022, *ApJL*, 938, L7
 Di Gesu, L., Marshall, H. L., Ehlert, S. R., et al. 2023, *NatAs*, 7, 1245
 Ehlert, S. 2023, AAS Meeting, 55, 336.02
 Ehlert, S. R., Liodakis, I., Middei, R., et al. 2023, *ApJ*, 959, 61
 Fossati, G., Maraschi, L., Celotti, A., Comastri, A., & Ghisellini, G. 1998, *MNRAS*, 299, 433
 HI4PI Collaboration, Bekhti, N., Flöer, L., et al. 2016, *A&A*, 594, A116
 Hovatta, T., & Lindfors, E. 2019, *NewAR*, 87, 101541
 Hu, X.-K., Yu, Y.-W., Zhang, J., et al. 2024, *ApJL*, 970, L22
 Kim, D. E., Di Gesu, L., Liodakis, I., et al. 2024, *A&A*, 681, A12
 Lynden-Bell, D. 1969, *Natur*, 223, 690
 Pandey, J. C., Singh, S., Yadav, R. K. S., et al. 2023, *JAI*, 12, 2240008
 Ramaprakash, A. N., Gupta, R., Sen, A. K., & Tandon, S. N. 1998, *A&AS*, 128, 369
 Rautela, B. S., Joshi, G. C., & Pandey, J. C. 2004, *BASI*, 32, 159
 Rybicki, G. B., & Lightman, A. P. 1986, *Radiative Processes in Astrophysics* (New York: Wiley)
 Schmidt, G. D., Elston, R., & Lupie, O. L. 1992, *AJ*, 104, 1563
 Shakura, N. I., & Sunyaev, R. A. 1973, *A&A*, 24, 337
 Tody, D. 1986, *Proc. SPIE*, 627, 733
 Tody, D. 1993, in ASP Conf. Ser. 52, *Astronomical Data Analysis Software and Systems II*, ed. R. J. Hanisch, R. J. V. Brissenden, & J. Barnes (San Francisco, CA: ASP), 173
 Ulrich, M.-H., Maraschi, L., & Urry, C. M. 1997, *ARA&A*, 35, 445
 Urry, C. M., & Padovani, P. 1995, *PASP*, 107, 803
 Wagner, S. J., & Witzel, A. 1995, *ARA&A*, 33, 163
 Weisskopf, M. C., Soffitta, P., Baldini, L., et al. 2022, *JATIS*, 8, 026002